GFD 2017 Lecture 6: Ocean Circulation beneath Ice Shelves

Adrian Jenkins; notes by Thomasina Ball and Robert Fajber

October 23, 2019

1 Insights from Plume Theory

1.1 Impact of meltwater outflow at the grounding line

Near the grounding lines of i ce shelves and tidewater glaciers there i s often an outflow of freshwater. The buoyancy flux from this meltwater will initially dominate over buoyancy due to melting to form a simple plume. As shown in figure1, the plume rises up the ice face entraining the ambient more saline water. This supplies heat which drives melting of the ice face adding further buoyancy to the plume and in turn driving the flow. The generation of meltwater at the grounding line can be due to a combination of factors. For glaciers in polar regions, geothermal heating and frictional heating causes melting at the base of the glacier, which drains through to the grounding line. In contrast, for more temperate glaciers, the freshwater is generated by surface melting and rain which drains to the base of glacier and then flows along to the grounding line.

We consider the full model derived in the previous lecture [3] that describes the conservation of mass, momentum, heat, and salt, respectively,

$$\frac{d}{dX}\left(DU\right) = \dot{e} + \dot{m}, \tag{1}$$

$$\frac{d}{dX}\left(DU^2\right) = D\Delta\rho g \sin\alpha - C_d U^2, \tag{2}$$

$$\frac{d}{dX}\left(DUT\right) = \dot{e}T_a + \dot{m}\left[T_b - \frac{L}{c}\right], \tag{3}$$

$$\frac{d}{dX}\left(DUS\right) = \dot{e}S_a + \dot{m}S_i, \tag{4}$$

where subscripts i, a and b are for water properties evaluated in the ice, ambient and at the ice-ocean boundary, respectively; α is the slope angle, and C_d is the drag coefficient. The entrainment is assumed proportional to the speed of the plume and written as $\dot{e} = E_0 U \sin\alpha$. By defining the density contrast $\Delta\rho$ and thermal driving ΔT of the plume as

$$\Delta\rho = \beta_S(S_a - S) - \beta_T(T_a - T), \tag{5}$$

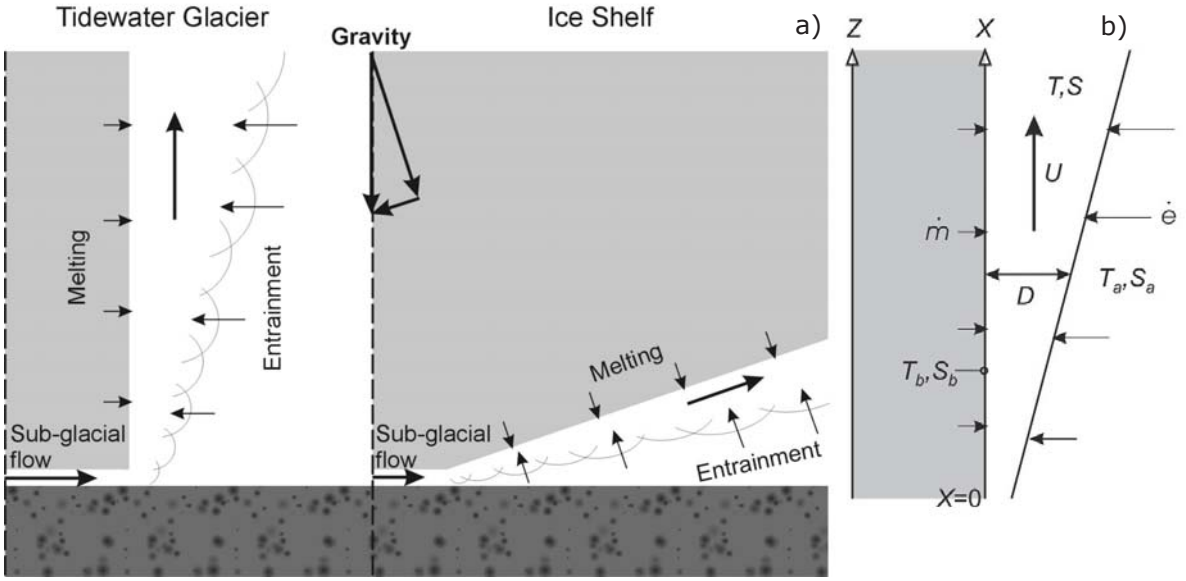

Figure 1: (a) Diagram of a plume originating from a flow of freshwater at the grounding line. (b) Schematic of the plume model with key variables indicated. From [3].

$$\Delta T = T - T_f \quad \text{where} \quad T_f = \lambda_1 S + \lambda_2 + \lambda_3 Z_b, \tag{6}$$

and using equations (1-4), evolution equations for the buoyancy and sensible heat flux can be found,

$$\frac{d}{dX}\left(DU\Delta T\right) = (T_a - T_{af})\dot{e} + (T_i^{ef} - T_{if})\dot{m} - (\lambda_3 \sin\alpha)DU, \tag{7}$$

$$\frac{d}{dX}\left(DU\Delta\rho\right) = \left(\frac{d\Delta\rho_a}{dZ}\sin\alpha\right)DU + \Delta\rho_i^{ef}\dot{m}, \tag{8}$$

where $T_i^{ef} = T_f - \frac{L}{c} - \frac{c_i}{c}(T_f - T_i)$ is the effective meltwater temperature and $\Delta\rho_i^{ef} = \beta_S(S_a - S_i) - \beta_T(T_a - T_i^{ef})$ is the effective meltwater density contrast.

When the flow of freshwater at the grounding line is large, the initial buoyancy flux dominates the flow, and hence, terms involving feedback due to melting can be neglected (e.g. setting $\dot{m} = 0$ in equations (1, 2, 7, 8)). In an unstratified ambient ocean, $d\Delta\rho_a/dZ = 0$, and neglecting the pressure dependence on the freezing point, $\lambda_3 = 0$, there is a simple solution where the plume increases linearly in thickness and all other parameters remain constant. Substituting in ansatz $D = AX^d$, $U = BX^u$, $\Delta\rho = CX^p$ and $\Delta T = DX^t$ results in $d = 1$, $u = 0$, $p = -1$ and $t = 0$. Hence, the solution is given by

$$U_0 = \left(\frac{B_0 \sin\alpha}{E_0 \sin\alpha + C_d}\right)^{1/3}, \quad D = E_0 \sin\alpha X, \quad B_0 = gD_0U_0\Delta\rho_0$$

$$(T - T_f)_0 = \left(\frac{E_0 \sin\alpha}{E_0 \sin\alpha + C_d^{1/2}\Gamma}\right)(T_a - T_{af}). \tag{9}$$

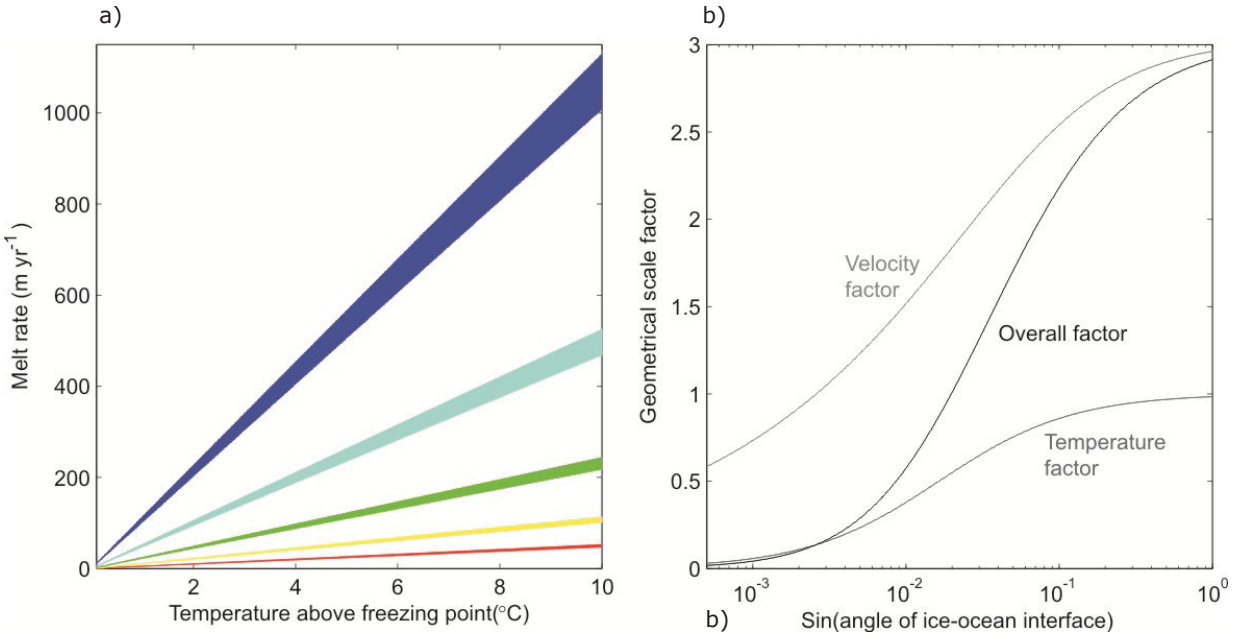

Figure 2: (a) Melt rate $\dot{m}$ plotted against thermal driving showing the linear relationship. The line width represent the spread of gradients for a the range of salinities from 25-35. (b) The geometrical factors, the second and third factors in melt rate in equation 11, plotted against the slope of the ice-ocean interface demonstrating the strong dependence on geometry. From [3].

The melt rate is then derived from the heat balance at the ice-ocean interface where the sensible heat is balanced by the heat flux from the plume mixture,

$$\dot{m}_0 L + \dot{m}_0 c_i (T_f - T_i) = c C_d^{1/2} U_0 \Gamma_T (T - T_f)_0. \tag{10}$$

Rearranging and substituting in U_0 and $(T - T_f)_0$ from equation (9) then gives the constant melt rate as

$$\dot{m}_0 = \left(\frac{c C_d^{1/2} \Gamma}{L + c_i (T_f - T_i)} \right) \left(\frac{\sin\alpha}{E_0 \sin\alpha + C_d} \right)^{1/3} \left(\frac{E_0 \sin\alpha}{E_0 \sin\alpha + C_d^{1/2} \Gamma} \right) B_0^{1/3} (T_a - T_{af}). \tag{11}$$

The melt rate in equation 11 is made up of several factors. The first factor is made up of physical constants such as the drag coefficient, heat capacity, transfer coefficients and the latent heat of fusion for ice. The second and third factors come from the dependence of the velocity and temperature gradient on the slope of the interface. The fourth and fifth factors identify the linear dependence on the thermal driving from the ambient ocean and the cube root dependence on the buoyancy flux, see figure 2.

The approximations made thus far allow progress to be made analytically but are unrealistic in terms of modeling plume dynamics at the ice-ocean interface. Therefore, the ambient stratification, increasing freezing point with depth and feedback from melting need to be included. The full system given by equations (1, 2, 7, 8) can be normalised by the scales

found in equation (9). A scale for the along slope distance X can be found by considering the lengthscale over which melting balances the initial amount of buoyancy from the grounding line,

$$L_0 = \frac{B_0}{\dot{m}_0 \Delta\rho_i^{ef} g}. \tag{12}$$

1.2 Impact of ambient properties

Ambient conditions can also be important in the plume dynamics. Figure 3 shows dimensionless solutions for the melt rate, volume flux, momentum flux, thermal driving, buoyancy flux, and sensible heat flux against the distance along slope for increasing stratifications. Consider first the unstratified case (red line in figure 3). As the plume rises, entrainment of the ambient ocean provides heat to keep the plume above the freezing point, with more heat required as the volume flux increases. However, as the plume rises the freezing point increases and in turn decreases the sensible heat flux; the ambient thermal driving can be seen to fall almost linearly as a result. There is a transition from melting to freezing when the thermal driving equals zero. As thermal driving continues to decrease all of the meltwater is subsequently refrozen. As the ambient stratification is increased, towards the purple line, the buoyancy flux reaches its maximum further downslope and hence loses momentum before all of the meltwater has frozen out. By increasing the stratification further, the section of freezing can be reduced to zero before the plume runs out of momentum.

The importance of the ambient conditions can be summarised in two key lengthscales. The first is the lengthscale over which the plumes' buoyancy changes and can be written as

$$L_{\rho a} = \frac{\Delta\rho_0}{(d\Delta\rho/dZ)\sin\alpha}. \tag{13}$$

The second is the lengthscale over which thermal driving changes,

$$L_{tf} = \frac{(T - T_f)_0}{\lambda_3 \sin\alpha}, \tag{14}$$

initially recognised by [6] to be an important lengthscale characterizing the distance from the source to the ambient freezing point.

Slater *et al* [10] looked at the importance of lengthscale $L_{\rho a}$ when the plume buoyancy is dominated by subglacial discharge, and hence feedback from submarine melting on the plume can be neglected, and $L_{TF} = \infty$. Initially they considered a uniform stratification, $L_{\rho a} = \infty$, and found that melt rate scaled with $B_0^{1/3}$ regardless of plume geometry providing discharge was below a critical value. This is consistent with the results derived above in equation (11). The addition of temperature stratification increased the sensitivity of the plume temperature to subglacial discharge. However, when the initial buoyancy at the grounding line is taken to be a point source the temperature in the plume becomes independent of discharge and so they found the exponent to be only slightly different from 1/3. Finally, if the salinity or temperature and salinity set the stratification, the melt rate exponent can vary from 1/3 to as large as 2/3 depending on other plume conditions. These higher exponents suggest that melt rates may depend more on subglacial discharge than previously thought.

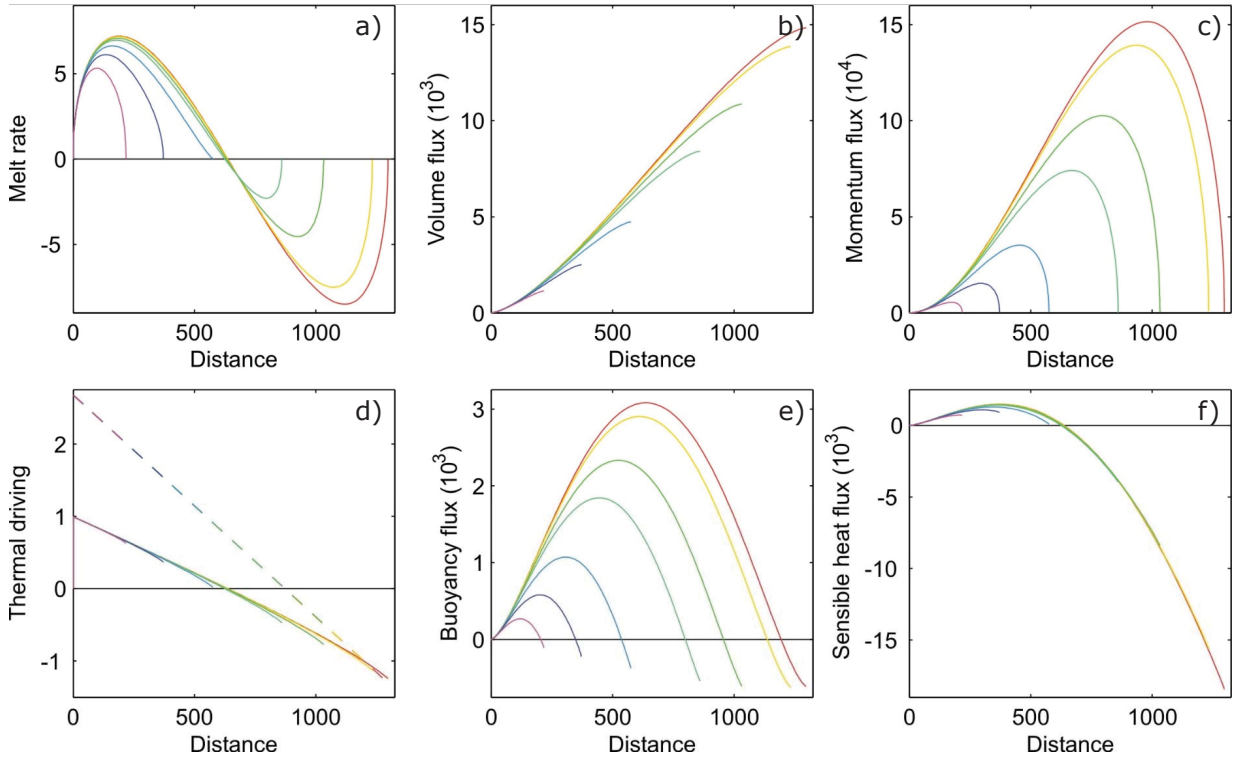

Figure 3: Change in plume dynamics depending on the ambient stratification. Dimensionless solutions for (a) melt rate, (b) volume flux, (c) momentum flux, (d) thermal driving, (e) buoyancy flux and (f) sensible heat flux plotted against distance along slope from the grounding line for an initial fresh water flux of $5 \times 10^{-5}\mathrm{m}^2\mathrm{s}^{-1}$ with slope $\sin\alpha = 0.01$. Colored lines indicate varying ambient stratification with zero stratification given by the red line and ambient stratification of $-1 \times 10^{-6}\mathrm{m}^{-1}$ given by the purple line. From [3].

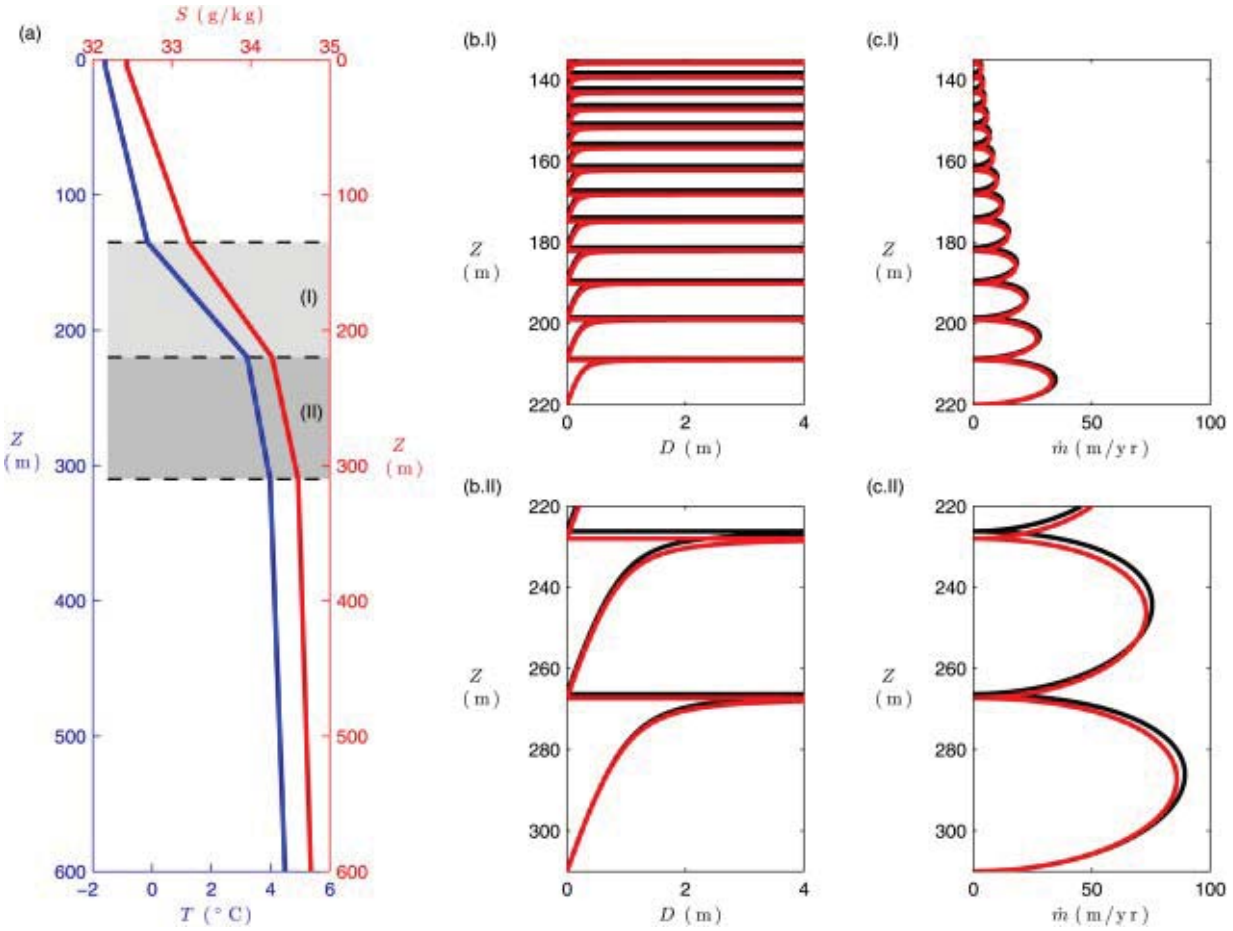

Figure 4: Case study of Helheim glacier in Sermelik fjord. (a) Linear approximation to change in temperature (blue line) and salinity (red line) with depth motivated by observations. Variation of width (bI and bII) and melt rate (cI and cII) with depth for the two regions shaded in grey in (a). From [7].

Conversely, Magorrian and Wells [7] studied the case when the initial discharge at the grounding line is zero and the buoyancy is dominated by meltwater from the ice-ocean interface, again with $L_{TF} = \infty$. They applied their theoretical and numerical results to a case study of melting of Helheim glacier in Sermelik fjord, Greenland, in winter, see figure 4. The numerical solution showed a repeated layered intrusion pattern as the plume reached its neutral buoyancy and the width d diverged. Further melting at the ice-ocean interface then starts the next intrusion. They argue that the layered melting pattern would lead to the formation of notches on the ice-ocean interface. As the depth decreases, the temperature and salinity decreases reducing thermal driving and melt rate causing the layered scaling to decrease, as seen in figure 4.

To identify when the governing lengthscales become important, the size of the lengthscale can be plotted against the thermal driving, temperature above the freezing point. Figure (5) compares the three lengthscales given in equations 12, (13) and (14) for an ice shelf and a

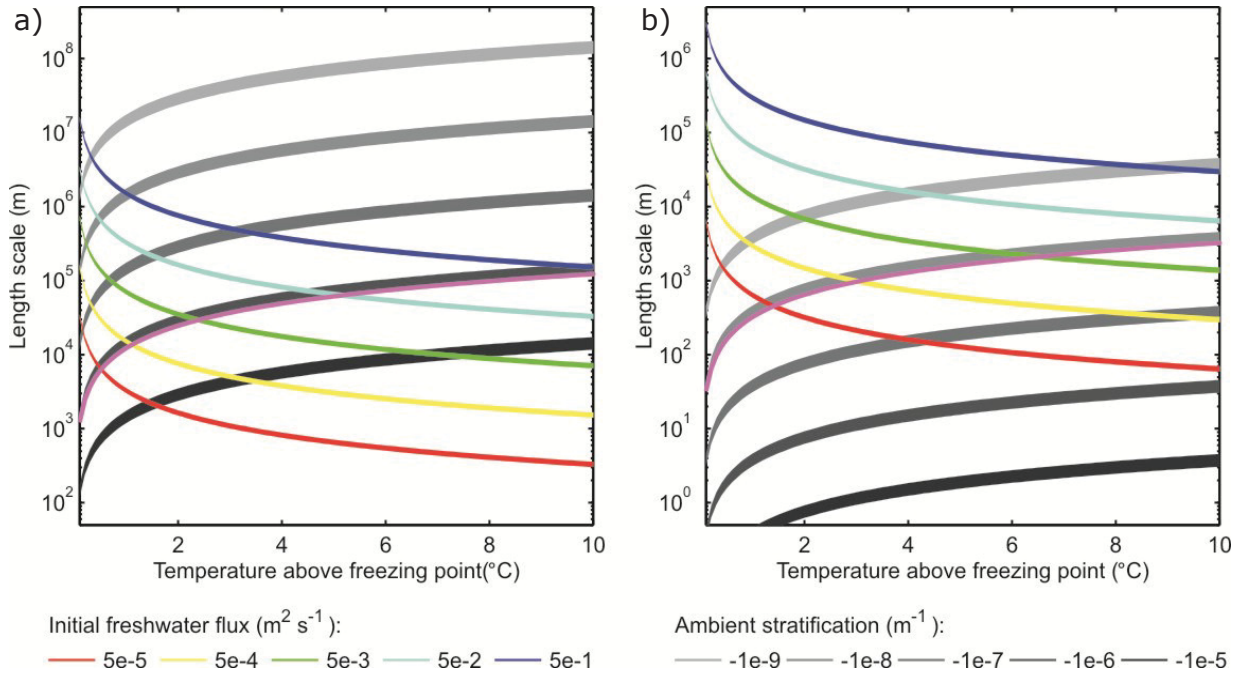

Figure 5: Governing lengthscales for a plume flowing upslope along an ice-ocean interface of slope (a) $\sin\alpha = 0.01$ (ice shelf grounding line) and slope (b) $\sin\alpha = 1$ (tidewater glacier). The coloured lines are plots of L_0 for different initial freshwater fluxes, the grey lines are $L_{\rho a}$ for a range of ambient stratifications, and the magnenta line is L_{TF}. From [3].

tidewater glacier. For the ice shelf, 5(a), other than the strongest stratification (black line), L_{TF} is the first lengthscale that becomes important for scales of hundreds of metres to tens of kilometres. Below this lengthscale the approximation of a plume in an unstratified environment, with freezing temperature independent of depth and no feedback from melting on the buoyancy of the plume is valid; see section 1.1. For a tidewater glacier, 5(b), entrainment is more important with the strongest stratification limiting the approximation in section 1.1 to tens of metres.

Slater *et al* [10] and Magorrian and Wells [7] both looked at the role of $L_{\rho a}$ in plume evolution. To consider the impacts of L_{TF} we need to return to the full model. We can run the model for a range of basal slopes from 10^{-3} to 10^{-2} with a grounding line depth of 500m and ambient water temperatures from 0 to 7C above the surface freezing point to get a series of melt rate curves. Figure 6(b) shows these melt rates where the evolution of the plume is stopped by the plume reaching the surface (termination of the ice shelf).

From the lengthscale recognised by Lane-Serff [6], see equation (14), one can see that the plume dynamics are unchanged by a linear transformation of the ambient temperature profile. Thus, we can construct equivalent ambient temperature profiles with a surface temperature fixed at T_f by varying grounding line from depths of 500m to 10000m. Running the model for these new profiles produces a series of melt rates given in figure 6(c), where again the solution is stopped by reaching the ice shelf edge.

In order to understand the role of lengthscales in the problem we would like to collapse

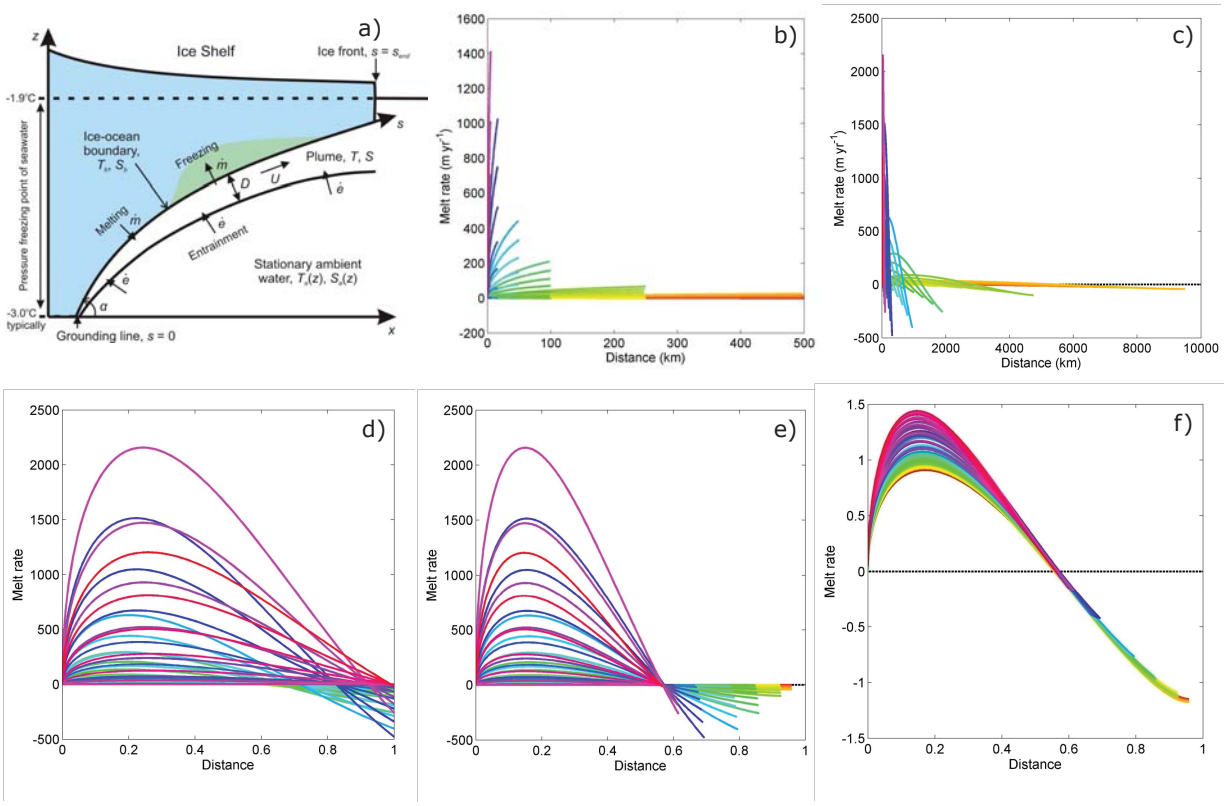

Figure 6: (a) Schematic of full solution. (b) Melt rate against (m/yr) against horizontal distance away from the grounding line for a range of ice shelves with a grounding line (km) depth of 500m, basal slopes from 10^{-3} to 10^{-2} and ambient ocean temperatures from 0 to 7C. (c) Melt rate (m/yr) against distance away from the grounding line (km) for a fixed surface freezing point temperature and grounding line depths from 500m to 10000m. (d) Melt rate (m/yr) against dimensionless distance away from the grounding line. (e) Melt rate (m/yr) for a rescaled dimensionless distance away from the grounding line. (f) Dimensionless melt rate against dimensionless distance away from the grounding line. See section 1.2.

all of the lines onto a universal curve by scaling the melt rate and distance from the origin suitably. By scaling the distance by L_{TF} the graph transforms to 6(d). Here the transition between melting and refreezing doesn't coincide exactly for all curves because the balance between entrainment and melting is a function of the basal slope. Rearranging equation (3) we have

$$DU\frac{dT}{dX} = \dot{e}T_a + \dot{m}\left[T_b - \frac{L}{c}\right] - (\dot{e}+\dot{m})T. \tag{15}$$

By balancing the heat due to entrainment and latent heat that goes into melting we can get a scaling for the thermal driving,

$$E_0 U \sin\alpha(T_a - T) - C_d^{1/2} U \Gamma_T (T - T_b) \simeq 0,$$

$$\Rightarrow (T - T_b) \simeq \frac{E_0 \sin\alpha}{C_d^{1/2}\Gamma_T + E_0 \sin\alpha}(T_a - T_b). \tag{16}$$

The prefactor here allows us to rescale L_{TF} such that the transition between melting and freezing is the same for each run, see figure 6(e).

Finally, the melt rate scaling comes from the plume speed and thermal driving. From equation (2) we have

$$DU\frac{dU}{dX} = D\Delta\rho g \sin\alpha - C_d U^2 - (\dot{e}+\dot{m})U. \tag{17}$$

By balancing the momentum due to plume buoyancy with entrainment and friction, we can get a scaling for plume velocity,

$$U^2 \simeq \frac{\sin\alpha}{C_d + E_0 \sin\alpha} D\Delta\rho g. \tag{18}$$

By considering the remainder of the thermal driving budget we have

$$(T_a - T) \simeq \frac{C_d^{1/2}\Gamma_T}{C_d^{1/2}\Gamma_T + E_0 \sin\alpha}(T_a - T_b), \tag{19}$$

which can be used to scale the buoyancy $\Delta\rho$. Hence, this finally allows the solutions to collapse on to one universal curve, see figure 6(f).

1.3 Adding further processes

The model investigated thus far has only considered the refreezing of meltwater at the ice-ocean interface. In reality, freshwater can freeze in the plume in the form of suspended disc-shaped frazil ice crystals [5]. This increases the buoyancy and causes the plume to accelerate which in turn promotes rapid crystal growth creating a positive feedback. If the ice crystals are able to deposit out in a manner opposite to sedimentation this reduces the bulk density causing the plume to decelerate and hence allowing crystals to settle out more easily. The formation of frazil ice comes in intense bursts that settle out in discrete intervals. These high rates of accumulation on the order of 1m/yr then give a mechanism for creation of thick layers of marine ice beneath ice shelves [1].

The coupling between ice shelf geometry and plume flow can also provide a mechanism for positive feedback. Le Brocq *et al* [2] used satellite imagery to show that channelisation often forms on the base of ice shelves. They found that these channels coincide with the predictions of outflow locations of freshwater at the grounding line. This suggests that meltwater plumes create ice-shelf channels which in turn focus plume flow promoting further melting in the channels. These features have been explored numerically in the form of 2D fully coupled ice-shelf/sub-ice shelf ocean models [9], which has shed light on the dynamics involved in the formation of these channels. However, plume models have yet to be able to simulate realistic circulation and melt rates beneath ice shelves.

2 Models of the 3D Circulation within a Cavity

2.1 Structure normal to the ice-ocean interface

To study the structure of the circulation normal to the ice-ocean interface, a simplified version of the rotated viscous Boussinesq equations are used. Since the focus is on the vertical structure, the gradients along the shelf are assumed to vanish, which eliminates the horizontal advection and diffusion terms. This leaves

$$\frac{\partial u}{\partial t} - \phi v = \Delta\rho g \sin\alpha - gcos\alpha \frac{\partial \eta}{\partial x} + \frac{\partial}{\partial z}\left(\nu \frac{\partial u}{\partial z}\right), \tag{20}$$

$$\frac{\partial v}{\partial t} + \phi u = -g\cos\alpha \frac{\partial \eta}{\partial y} + \frac{\partial}{\partial z}\left(\nu \frac{\partial u}{\partial z}\right), \tag{21}$$

where η is the deviation of the ice-ocean interface from its equilibrium position, and ϕ is the Coriolis parameter in the rotated system. Under the same assumptions the equations for conservation of energy and salinity become

$$\frac{\partial T}{\partial t} = \frac{\partial}{\partial z}\left(\kappa_T \frac{\partial T}{\partial z}\right), \tag{22}$$

$$\frac{\partial S}{\partial t} = \frac{\partial}{\partial z}\left(\kappa_S \frac{\partial S}{\partial z}\right). \tag{23}$$

By linearizing the dependence of the freezing temperature on salinity and pressure, the thermal driving can be expressed as

$$T_* = T - (\lambda_1 S + \lambda_2 + \lambda_3 P(\eta)), \tag{24}$$

and applying equation (24) with equations (23) allows us to write a conservation equation for thermal driving as

$$\frac{\partial T_*}{\partial t} = \frac{\partial}{\partial z}\left(\kappa \frac{\partial T_*}{\partial z}\right).$$

In order to simplify the analysis throughout this section, we will take $\nu = \kappa$ and make κ a fixed constant. To relate T_* to buoyancy, we will use equation (7).

Equations (7) and (24) can be used to write a simple expression for the ratio of the density difference to the difference in thermal driving due to melting of ice into the plume

$$\frac{\Delta\rho}{\Delta T_*} = \frac{S_a\beta_S - \beta_T\left[T_{*a} + \left(L_i - c_i T_{*i}\right)c_w^{-1}\right]}{T_{*a} + (L_i - c_i T_* i)c_w^{-1} - S_a\lambda_1}.$$

Note that the expression includes both the enthalpy required to reduce the ice to the freezing point temperature and the latent heat.

Requiring that the solutions are in equilibrium with the ice-ocean interface (no slip momentum condition and at the freezing point) implies an upper boundary condition of

$$\mathbf{u} = 0,\ \mathrm{T}_* = 0 \text{ at } z = 0 \tag{25}$$

. Since we are interested in studying the boundary layer near to the ice-ocean interface we will consider solutions that decay to the ambient conditions in the far field. Taking the ambient flows to be in geostrophic balance, this gives the lower boundary of

$$\mathbf{u} = \frac{ig\nabla\eta}{\phi},\ T_* = T_{*a} \text{ at } z = -\infty. \tag{26}$$

Similar equations have been used to describe the flow of dense currents down a continental slope. Here, however, the top condition is to fix the temperature to the freezing point, a Dirichlet boundary condition, instead of the zero flux Neumann boundary condition that would be applied at the seabed.

In order to get a lengthscale to normalize the solutions, we start by calculating the Ekman depth for the system. By looking for stationary solutions at the ambient density with the ice-ocean interface at its equilibrium position equations (21) become

$$\begin{aligned} -\phi v &= \kappa\frac{\partial^2 u}{\partial z^2}, \\ \phi u &= \kappa\frac{\partial^2 v}{\partial z^2}. \end{aligned}$$

These have the well known (bottom layer) Ekman solution:

$$\begin{aligned} u &= v_g^i exp\left(-\frac{z}{d_E}\right) sin\left(\frac{z}{d_E}\right), \\ v &= v_g^i exp\left(-\frac{z}{d_E}\right) cos\left(\frac{z}{d_E}\right), \end{aligned}$$

with relevant scales

$$v_g^i = \frac{g}{\phi} sin\alpha \frac{\Delta\rho}{\Delta T_*}, \tag{27}$$

$$d_E = \sqrt{\frac{2\kappa}{|\phi|}}. \tag{28}$$

$$\tag{29}$$

The depth scale is the e-folding distance of the boundary layer. The velocity scale is the geostrophic current that would occur in the absence of friction along the ice-ocean interface. This is why it is T_*a and not T_* that appears in u_g^i. When the slope is small, the Coriolis parameter $\phi \approx 2\Omega sin\theta cos\alpha$ and the velocity scale is, incidentally, the same as the Nof speed, which describes the translation of cold eddies along a sloped bottom. The temperature scale is simply chosen to be the thermal driving of the ambient system, T_{*a}.

The solution to this system for some simple cases is given in figure 7. The thermal driving is shown in panels (a) and (d); the solution shows the diffusion of cold water into the far field. This produces a gradually weakening stratification. If a finite domain was used, equation (24) with a constant diffusivity would imply that the steady state solution is just a linear profile joining the thermal driving at the ice-ocean interface and the ambient thermal driving. This is why the transient solutions are studied, since the steady state solution (or the asymptotic solution in the case where the boundary condition is applied in the far field) does not permit a boundary layer.

Panels (b) and (e) show the velocity components of the system when a background pressure gradient is applied with a flat ice-ocean interface. A relatively shallow boundary layer is formed at the surface, and quickly converges to the Ekman solution. This is to be expected, since the Ekman solution is calculated without the influence of the sloped ice-ocean interface. When the ice interface slope is sloped, as in panels (c) and (f), the boundary layer thickens initially, and the cross slope currents do not appear to converge to the Ekman solution. When the ice interface is sloped, it introduces baroclinicity and links the thermal and current profiles. Thus, the impact of thermal diffusion will be felt on the currents in this case.

We can further explore impacts of the slope of the ice-ocean interface on the response of the boundary layer current by decomposing the long term response of the boundary layer with and without a sloped interface (figure 7, panels (e) and (f), respectively) into geostrophic and ageostrophic components (figure 8). This is done by assuming that the geostrophic current is time dependent and in the cross shelf direction:

$$\phi v_g = \Delta\rho g sin\alpha, \tag{30}$$

$$\frac{\partial v_g}{\partial t} = \nu \frac{\partial^2 v_g}{\partial z^2}. \tag{31}$$

The time dependence results from the diffusion of less buoyant water away from the ice-ocean interface. This is shown in panels (b) and (e) of figure 8. In the case without a slope in the ice-ocean interface, the geostrophic component has no vertical shear, since the applied forcing is barotropic. In the case with a sloped ice interface condition the geostrophic component shows a vertical structure, in thermal wind balance with the applied baroclinic forcing. The ageostrophic components are assumed to be time independent, and can be shown to the same as the Ekman solution (27). Thus the frictional boundary layer response is unaffected by whether a barotropic or baroclinic forcing is applied to the system (panels (e) and (f) in figure 8).

In general the total response will be a combination of the frictional boundary layer, the applied barotropic and baroclinic forcings, and the ice shelf geometry. For instance, if the baroclinic forcing is chosen to oppose the barotropic forcing, the results can stop or even reverse the upslope current (u) near the ice-ocean interface. For a finite cavity, curvature in

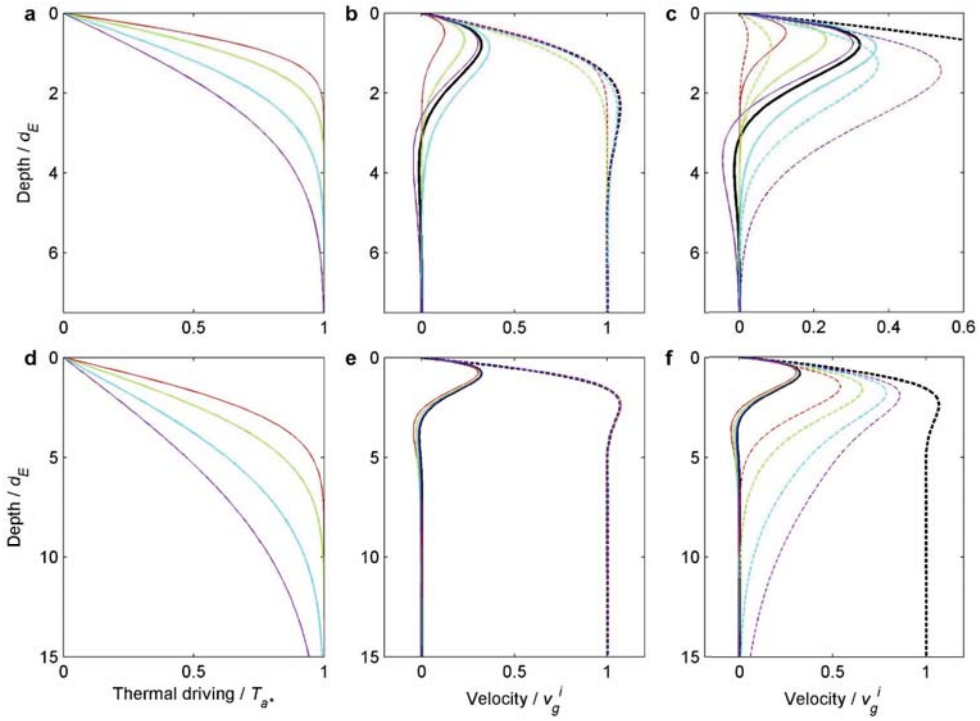

Figure 7: The thermal driving, (a) and (d), and boundary layer currents, (b),(c),(e) and (f), for two simple cases described in the text. The solid lines in (b),(c),(e) and (f) correspond to the up slow flow (u) and the dashed lines correspond to across slope flow. In the top row is the transient solution after 0.1 (red), 0.2(green), 0.5(cyan) and 1.0(magenta) inertial periods, and the bottom row is the transient solution after 1.0 (red), 2.0(green), 5.0(cyan) and 10.0 (magenta) inertial periods, $T = \frac{2\pi}{f}$. The black lines show the Ekman solution obtained from (29). From [4]

the sea floor bottom, h, can also create a current that can oppose the barotropic forcing and oppose the upslope flow, since the planetary vorticity is $\frac{\phi}{h}$.

Another interesting regime occurs when it is assumed that the upslope density gradient balances the turbulent diffusion of upslope momentum instead of the Coriolis term that balances it in the Ekman regime. The density gradient is assumed to be replenished by advection from a steady state upslope current. This results in a solution similar to the Prandtl model of the Katabatic wind

$$-g \sin\alpha \Delta\rho = \kappa \frac{\partial^2 u}{\partial z^2}, \tag{32}$$

$$\frac{\partial \Delta\rho}{\partial x} = \kappa \frac{\partial^2 \Delta\rho}{\partial z^2}. \tag{33}$$

which has solutions

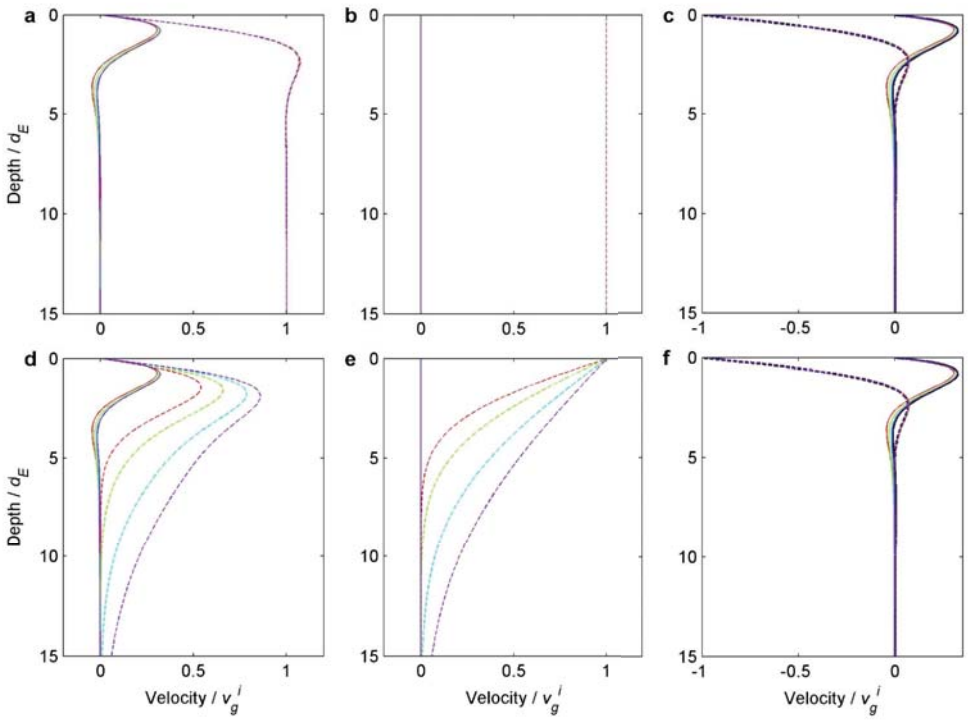

Figure 8: The decomposition of panels (e) (top row) and (f) (bottom row) into their geostrophic (middle column) and ageostrophic (right column) components. The times and current directions indicated by the lines are the same as in panels (e) and (f). From [4].

$$
\begin{aligned}
u &= u_p exp\left(-\frac{z}{d_P}\right) sin\left(\frac{z}{d_P}\right) \\
\Delta\rho &= \frac{\Delta\rho}{\Delta T_*} T_{*a} exp\left(-\frac{z}{d_P}\right) cos\left(\frac{z}{d_P}\right)
\end{aligned}
$$

where the scales are

$$
u_P = \left(\frac{g\sin\alpha}{\frac{\partial\Delta\rho}{\partial x}}\right)^{\frac{1}{2}} \frac{\Delta\rho}{\Delta T_*} T_{*a} \tag{34}
$$

$$
d_P = \left(\frac{4K^2}{g\sin\alpha\frac{\partial\Delta\rho}{\partial x}}\right)^{\frac{1}{4}} \tag{35}
$$

These solutions look similar to the Ekman solutions, but with a different scaling. Notably, ϕ no longer appears in the equations, but instead the horizontal buoyancy gradient, $\partial\Delta\rho/\partial x$ appears.

To determine whether the boundary layer will better resemble the Prandlt or Ekman solution, we note that $u_P\ exp(-z/dP)$ and $u_E\ exp(-z/d_E)$ so that $u_P \geq_E$ when $d_P \leq d_E$. This is true when

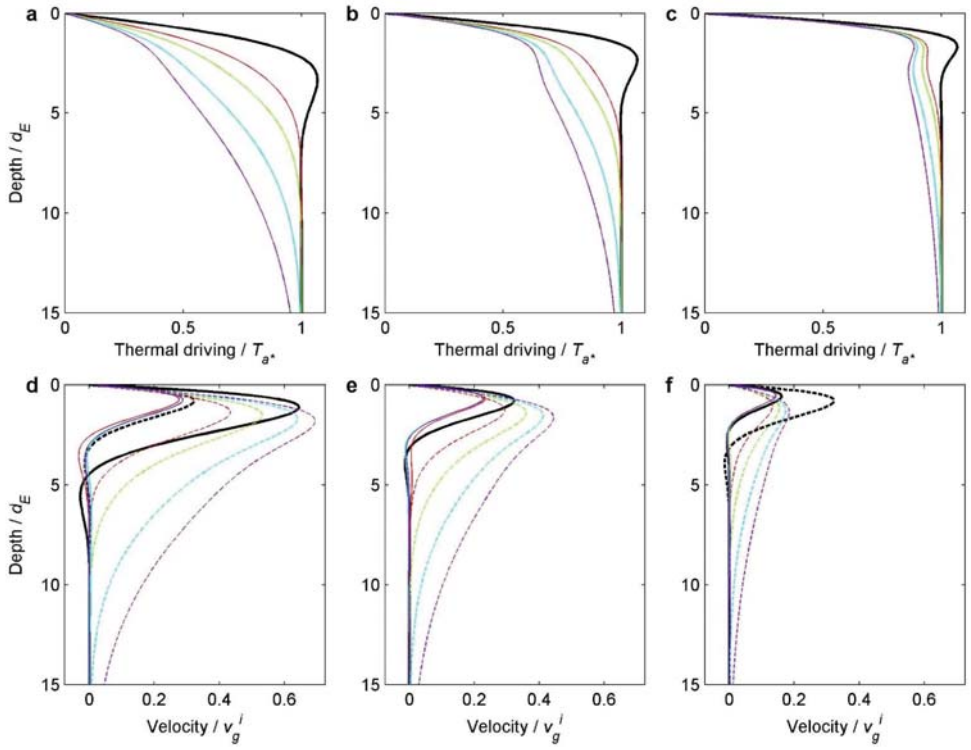

Figure 9: Top Row: the thermal driving for the case with $d_P/d_E = \sqrt(2)$, (left column), $d_P/d_E = 1$ (middle column), and $d_P/d_E = \sqrt{\frac{1}{2}}$ (right column). The black line is the theoretical Prandtl solution given by (35) The colors indicate the same time periods as in figure 8. Bottom Row: as for the top row, but now for the velocity components. The dashed black line is the theoretical Ekman solution, and the solid black line is the theoretical Prandtl solution. In the middle column they overlie each other. The colors indicate the same as in figure8. from [4]

$$\frac{\partial T_*}{\partial x} \geq \frac{\Delta T_*}{\Delta \rho} \frac{\phi^2}{g \sin \alpha} \tag{36}$$

or equivalently when

$$\left(g \frac{\partial \Delta \rho}{\partial z}\right) \left(\frac{sin\alpha}{\phi}\right)^2 \geq 1 \tag{37}$$

This last equation has the form of a Boundary Layer Burger number. Solutions to the full for a case with upslope temperature advection are shown in figure 9 for differing values of d_P/d_E. For low values of d_P/d_E the solution has a thick and strong boundary layer near the ice-ocean interface. When the values of d_P/d_E are higher, the boundary layer becomes thinner and sharper. The addition of the along slope temperature gradient allows for a maintained stratification in a thin layer near the surface. Since, typically, we expect that $\left(g \frac{\partial \Delta \rho}{\partial z}\right) > \phi^2$, and for an ice shelf with $\sin \alpha \approx 0$ we would expect the Ekman solution to be more appropriate. For $\sin \alpha \approx 1$ however the Prandtl solution might become appropriate.

The solutions shown in figure 7 panels (c) and (f) can also be compared with a model with a more realistic diffusivity from a parametrized turbulence closure scheme. We take

$$\nu = \lambda u_*, \tag{38}$$

$$u_* = \left(\nu \left|\frac{du}{dz}\right|\right)^{\frac{1}{2}}, \tag{39}$$

$$\lambda = min(\kappa_v u_*, \lambda_{max}). \tag{40}$$

This allows us to include the production of TKE from shear layers. Inspection of the solution with the scheme included (figure 10) reveals that the boundary layer becomes trapped in a layer near the surface.

2.2 From a 1d column to the 3d circulation

Now we consider what affects the finite geometry of a real cavity would have on the 1d model of the previous section. The pressure at any point in the fluid can be written as

$$P(z) = g\left[\int_{z_{io}+\eta}^{z_s+\eta} \rho_i dz + \int_z^{z_{io}+\eta} \rho dz\right], \tag{41}$$

and assuming that density of the ice is constant, we find that

$$\nabla P(z) = g\left[\rho_i \nabla H_i + \rho_{io} \nabla\left(z_{io}+\eta\right) + \int_z^{z_{io}+\eta} \nabla\rho dz\right]. \tag{42}$$

The first term is the contribution to pressure from the weight of the ice, the second term is the gradient in the ice-ocean interface (both the equilibrium position and the deviation), and the third is the is baroclinic contribution of the (assumed) density profile. Assuming that the weight of the ice shelf is balanced by the water in its equilibrium position, we can write the flotation condition as

$$\rho_i \nabla H_i + \rho \nabla z_{io} = 0. \tag{43}$$

Applying this equation to the model and solving it over a finite depth reveals a deep cross slope geostrophic flow and a second Ekman layer in the cavity along the seabed. This second Ekman layer creates a mass flux convergence along the grounding line. By conservation of mass, this would raise the ice shelf there and generate an opposing barotropic flow. For a semi-infinite ice sheet we can rationalize this by supposing that this flow is in the across shelf direction. However for an actual 2d dimensional cavity this paradox needs to be resolved differently.

In order to understand the structure of the circulation in the cavity we start by constructing a 2d idealized model of a steady state current in balance with the pressure gradients applied at the ice-ocean interface. This will allow us to understand the two-dimensional structure imposed by finite cavity geometry. We start by assuming that the momentum equations are in approximate geostrophic balance, with only the vertical momentum diffusion equation term retained:

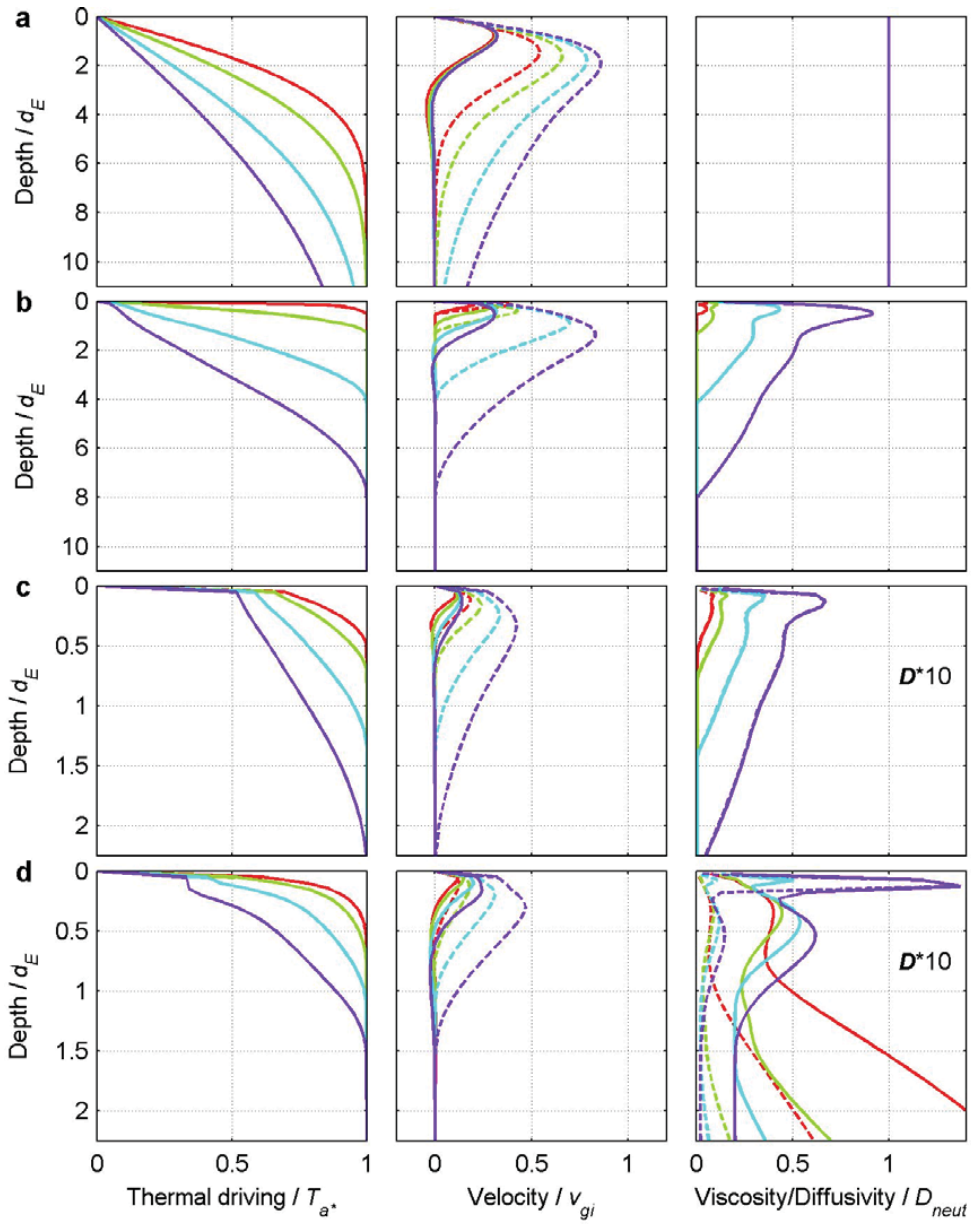

Figure 10: The solutions from a model using a parametrized turbulence closure scheme. The situation is the same as shown for figure 7, panels (c) and (f). The first row uses the scheme described in the text; going down rows the turbulence closure scheme increases in complexity.

$$-fv = -\frac{1}{\rho_0}\frac{\partial P}{\partial x} + \frac{\partial}{\partial z}\nu\frac{\partial u}{\partial z} \tag{44}$$

$$fu = -\frac{1}{\rho_0}\frac{\partial P}{\partial y} + \frac{\partial}{\partial z}\nu\frac{\partial v}{\partial z}. \tag{45}$$

$$\tag{46}$$

The inclusion of the vertical mixing terms allows us to retain the features of Ekman

solution that were studied in the previous section. The pressure is as given in (42) but with the flotation condition applied and the baroclinic term approximated by the equilibrium height of the ice-ocean interface:

$$\nabla P = g\left[\rho_0 \nabla\eta + \int_z^{z_{io}} \nabla\rho dz\right] \tag{47}$$

The depth integrated geostrophic flow is given by

$$V_g = \frac{g}{f}\mathbf{k} \times \left(H_w \nabla\eta + \int_z^{z_{io}} \nabla\rho\,(z - z_b)\,dz\right) \tag{48}$$

where H_w is the depth of the water column. The depth integrated ageostrophic velocity comes from the top and bottom Ekman layers and is given by

$$V_a = \frac{d_E}{2}\mathbf{k} \times (v_{gio} + v_{gb}) + \frac{d_E}{2}(v_{gio} + v_{gb}), \tag{49}$$

where the top and bottom geostrophic currents are given by

$$v_{gio} = \frac{g}{f}\mathbf{k} \times \nabla\eta, \tag{50}$$

and

$$v_{gb} = \frac{g}{f}\mathbf{k} \times \nabla\eta + \int_{z_b}^{z_{io}} \nabla\rho dz, \tag{51}$$

respectively. The first term in (49) is a transport normal to the geostrophic flow, and the second term is a transport in the along geostrophic flow created by a reduction in the geostrophic flow speed in the boundary layer.

Mass conservation implies that the divergence of these two currents has to vanish in steady state:

$$\nabla \cdot (\mathbf{V_g} + \mathbf{V_a}) = 0 \tag{52}$$

Substituting equations (48) and (49) into (52) and assuming a constant linear stratification (constant N^2) profile parallel to the ice shelf gives a second order hyperbolic equation for the deviation of the ice-ocean interface from its equilibrium position:

$$\begin{array}{rcl} \frac{g}{f}\left[\frac{\partial H_w}{\partial y}\frac{\partial \eta}{\partial x} - \frac{\partial H_w}{\partial x}\frac{\partial \eta}{\partial y}\right] + \frac{N^2}{f}H_w\left(\frac{\partial H_w}{\partial y}\frac{\partial z_i}{\partial x} - \frac{\partial H_w}{\partial x}\frac{\partial z_i}{\partial y}\right) & + & \\ \frac{g}{f}d_E\left[\frac{\partial^2 \eta}{\partial x^2} + \frac{\partial^2 \eta}{\partial y^2}\right] + \frac{N^2}{f}H_w\frac{d_E}{2}\left[\frac{\partial^2 z_i}{\partial x^2} + \frac{\partial^2 z_i}{\partial y^2}\right] & + & \\ \frac{N^2}{f}\frac{d_E}{2}\left[\frac{\partial H_w}{\partial x}\frac{\partial z_i}{\partial x} + \frac{\partial H_w}{\partial y}\frac{\partial z_i}{\partial y} - \frac{\partial H_w}{\partial y}\frac{\partial z_i}{\partial x} + \frac{\partial H_w}{\partial x}\frac{\partial z_i}{\partial y}\right] & = & 0 \end{array} \tag{53}$$

The first term represents the barotropic geostrophic flow caused by the ice ocean interface forced through depth contours. The second term is similar, it is the geostrophic flow being forced by the tilt of the sea level. The second two terms are the Ekman transports that result from the curvature of the ice ocean interface and the sea level, respectively. These terms are similar to the windstress forcing that would occur in an Ekman layer exposed to the atmosphere. The last term is a correction to the second term that results from the depth

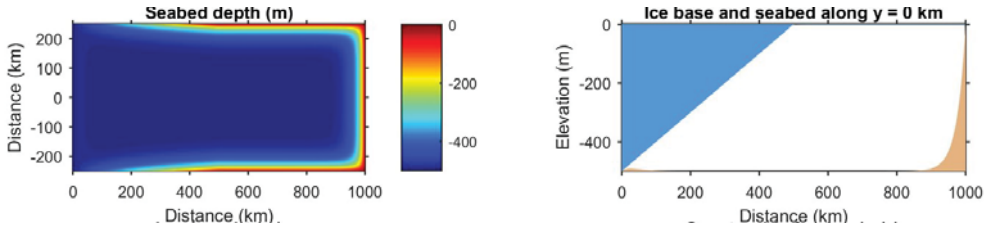

Figure 11: The simplified geometry used to test the circulation models. Left: the seabed depth and Right: a cross section showing the geometry of the ice shelf. Note that the bed has been tapered in order to avoid numerical artifacts.

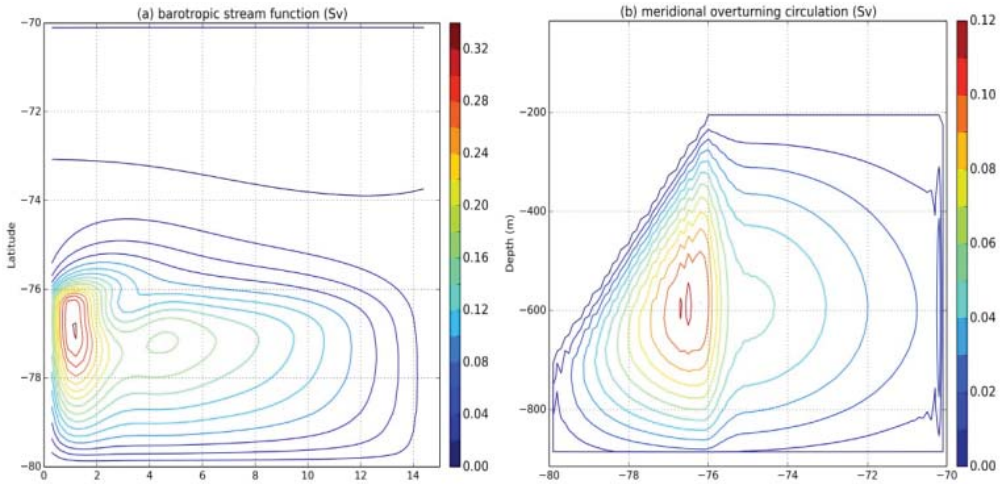

Figure 12: The barotropic streamfunction (left) and the meridional overturning circulation (right) from the primitive equation model using the same geometry show in figure 11. From [8].

of the Ekman depth. Over this depth part of the current in the second term will be canceled by the Ekman divergence, and this is accounted for in the last term.

If boundary conditions are given, this model can be solved for η. Using a simple test geometry (figure 11) this gives an asymmetric circulation, with increased sea heights on the bottom left side of the domain and decreased sea heights on the upper right side of the domain. It should be noted that since this calculation is done with an f-plane, this intensification is not related to the usual western boundary current intensification, and is instead related to the meridional gradient in water column thickness. These results compare favorably with a primitive equation model (NEMO) run with full physical parametrization (figure 12, left panel). The primitive equation model also shows the full three dimensional circulation, which shows a meridional overturning cell (figure 12, right panel) as well as a melt freeze pattern similar to an ice pump (figure 13). The gyre circulation is imprinted on the melt freeze pattern, and shifts the horizontal structure so that the melting is in the west, and the freezing in the east.

The full primitive equation model can be used to simulate the full circulation beneath all of the antarctic ice shelves, including observed bathymetry. The model simulation shows that

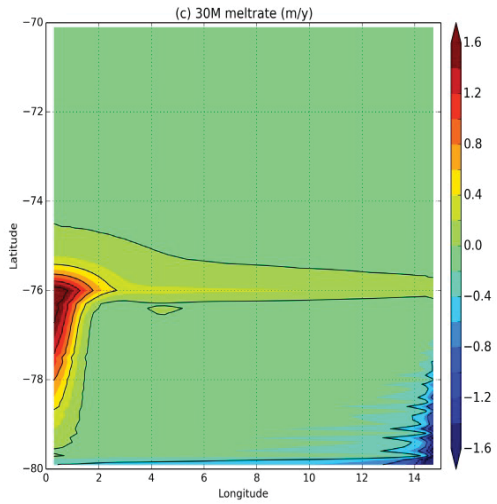

Figure 13: The freezing patterns from the primitive equation model, from [8].

the ice shelves in the warm regions of West Antarctica are rapidly melting (figure 14, panel (a)). In the cold water regions of the Ross and Weddell seas and also East Antarctica the melting occurs more slowly, and there are also extensive areas of refreezing (figure 14, panels (b), (c), and (d)). This model compares much better to observations than the plume model does in the area of the Ronne ice shelf. This is because the fully 3d model can simulate the buoyancy driven circulation that carries water away from melt zone, which is not included in the depth integrated plume model.

Sensitivity tests which involve removing the ice shelves show that there is a large influence of the ice shelves on sea ice formation. When the shelves are removed, large buildups of sea ice occur on West Antartica. This occurs because the melting of the land ice is introduced into the ocean at the surface in the grid cell nearest to the coast. This introduces a layer of fresh water at the surface that produces an unrealistically strong stratification, which prevents heat fluxes from the ocean from reaching the ice and an unrealistically thick layer of sea ice can form. The impact of the ice shelves is to input a similar amount of water as the land ice, but by inputing the water at depth, the ice shelves change the stratification and so do not allow such large regions of ice to grow. Similarly, melting of the shelves drives gyres within troughs in the continental shelf. These gyres can connect otherwise separate troughs, and also introduce cold fresh water fluxes at depth, which is critical to the formation of Antartic Bottom Water.

A caveat to these simulations is that the bathymetry is unknown in many circumstances. The areas where the bathymetry are the least well known are also the areas where the disagreement between the model and the observations are the largest. Improving the knowledge of the bathymetry could be a key step in our ability to simulate the circulation under the Antarctic ice shelves.

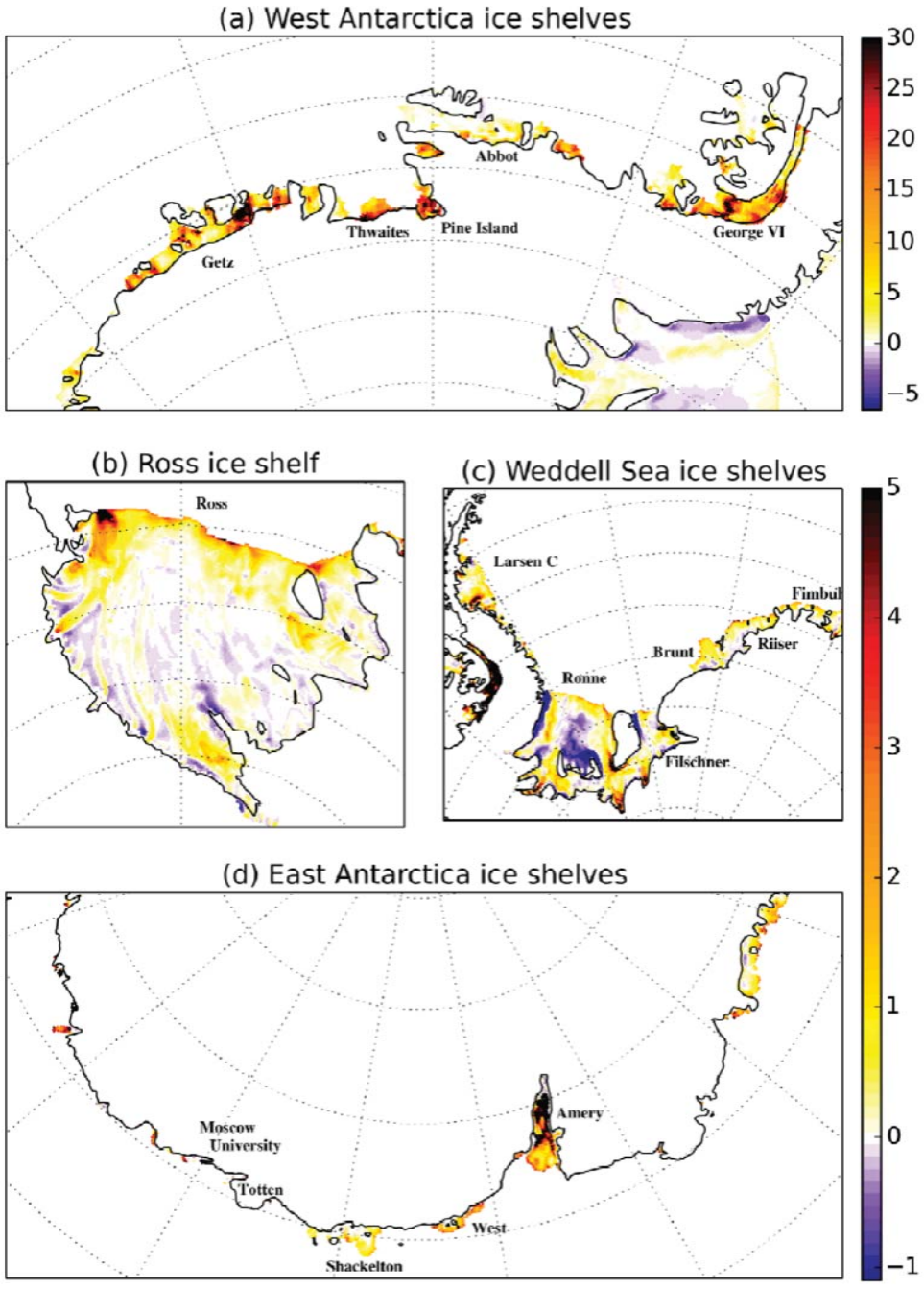

Figure 14: The melting patterns from the primitive equation model, run using observed bathemetry. From [8].

References

[1] A. Bombosch and A. Jenkins, Modeling the formation and deposition of frazil ice *beneath filchner-ronne ice shelf*, Journal of Geophysical Research: Oceans, 100 (1995), pp. 6983–6992.

[2] A. M. L. Brocq, N. Ross, J. A. Griggs, R. G. Bingham, H. F. J. Corr, F. Ferraccioli, A. Jenkins, T. A. Jordan, A. J. Payne, D. M. Rippin, and M. J. Siegert, *Evidence from ice shelves for channelized meltwater flow beneath the Antarctic Ice Sheet*, Nat. Geosci., 6 (2013), pp. 1–4.

[3] A. Jenkins, *Convection-Driven Melting near the Grounding Lines of Ice Shelves and Tidewater Glaciers*, Am. Meteorol. Soc., (2011).

[4] ——, *A simple model of the ice shelf–ocean boundary layer and current*, Journal of Physical Oceanography, 46 (2016), pp. 1785–1803.

[5] A. Jenkins and A. Bombosch, *Modeling the effects of frazil ice crystals on the dynamics and thermodynamics of ice shelf water plumes*, Journal of Geophysical Research: Oceans, 100 (1995), pp. 6967–6981.

[6] F. Lane-Serff, G, *On meltwater under shelves*, J. Geophys. Res., 100 (1995), pp. 6961–6965.

[7] S. J. Magorrian and A. J. Wells, *Turbulent plumes from a glacier terminus melting in a stratified ocean*, J. Geophys. Res. Ocean., 121 (2016), pp. 4670–4696.

[8] P. Mathiot, A. Jenkins, C. Harris, and G. Madec, *Explicit and parametrised representation of under ice shelf seas in a z* coordinate ocean model*, Geosci. Model Dev. Discuss, (in review).

[9] O. V. Sergienko, *Basal channels on ice shelves*, Journal of Geophysical Research: Earth Surface, 118 (2013), pp. 1342–1355.

[10] D. A. Slater, D. N. Goldberg, P. W. Nienow, and T. R. Cowton, *Scalings for Submarine Melting at Tidewater Glaciers from Buoyant Plume Theory*, Am. Meteorol. Soc., 46 (2016), pp. 1839–1855.